

Tunable Superlattice in Graphene To Control the Number of Dirac Points

Sudipta Dubey,[†] Vibhor Singh,[†] Ajay K Bhat,[†] Pritesh Parikh,^{†,§} Sameer Grover,[†]
Rajdeep Sensarma,[‡] Vikram Tripathi,[‡] K. Sengupta,[¶] and Mandar M.
Deshmukh^{*,†}

Department of Condensed Matter Physics and Materials Science, Tata Institute of Fundamental Research, Homi Bhabha Road, Mumbai 400005, India, Department of Theoretical Physics, Tata Institute of Fundamental Research, Homi Bhabha Road, Mumbai 400005, India, and Theoretical Physics Department, Indian Association for the Cultivation of Science, Kolkata 700032, India

E-mail: deshmukh@tifr.res.in

KEYWORDS: Graphene, Superlattice, Dirac points, band structure

Abstract

Superlattice in graphene generates extra Dirac points in the band structure and their number depends on the superlattice potential strength. Here, we have created a lateral superlattice in a graphene device with a tunable barrier height using a combination of two gates. In this Letter, we demonstrate the use of lateral superlattice to modify the band structure of graphene leading to the emergence of new Dirac cones. This controlled modification of the band structure persists upto 100 K.

^{*}To whom correspondence should be addressed

[†]Department of Condensed Matter Physics and Materials Science, Tata Institute of Fundamental Research, Homi Bhabha Road, Mumbai 400005, India

[‡]Department of Theoretical Physics, Tata Institute of Fundamental Research, Homi Bhabha Road, Mumbai 400005, India

[¶]Theoretical Physics Department, Indian Association for the Cultivation of Science, Kolkata 700032, India

[§]Birla Institute of Technology and Science, Pilani, Hyderabad, 500078, India

Chirality in graphene provides a unique platform for the experimental observation of phenomena like Klein tunneling,¹⁻³ unusual integer quantum Hall effect,^{4,5} and rich fractional quantum Hall spectra.^{6,7} The carrier density in graphene can be changed by applying gate voltages, which allows one to study tunable plasmonic and photonic excitations,⁸⁻¹² Coulomb drag¹³ along with technological applications¹⁴ like optical modulators,¹⁵ RF transistors,¹⁶ and ultrafast and high gain photodetectors.^{17,18} A technological challenge in working with graphene is the absence of a bandgap. Several methods like chemical functionalization,¹⁹ nanoribbons,²⁰ uniaxial strain engineering²¹ have been proposed and experimentally demonstrated to modify the band structure of graphene. However, ideas based on chemical functionalization, nanoribbons, and strain engineering do not provide any tunability of properties and their compatibility with large scale integration of devices is yet to be tested. Esaki et al.²² first proposed the use of a periodic superlattice (SL) potential to modify the band structure in semiconductors and similar experiments have been proposed in monolayer and bilayer graphene.²³⁻²⁹ In contrast to conventional materials, SL in graphene results in anisotropic renormalization of the velocities of the Dirac quasiparticles^{24,30} leading to the possibility of collimation.³¹ It also generates extra Dirac points^{23,24,32} in the band structure and these have been experimentally observed in graphene where the substrate induces a periodic potential.³³⁻³⁶ Superlattices using Moire pattern³⁷ by laying graphene over hexagonal boron nitride substrates³³ have been demonstrated, but they suffer from the lack of tunability of the superlattice potential. For the first time, here we have created a lateral SL in a graphene device with a tunable barrier height using a combination of two gates with the top-gate consisting of a comb like structure pinned to the same potential. An ability to engineer the band structure of graphene using SL, as we demonstrate, opens up new possibilities.

To achieve this goal we fabricate devices in Hall bar geometry with multiple thin top gates defined over the central region of graphene as shown in the schematic in Figure 1a. Figure 1b shows a scanning electron microscope (SEM) image of a device showing multiple (~ 27 nm wide) Pd top gates with a period of 150 nm (details in Section 1 of Supporting Information). The graphene flake

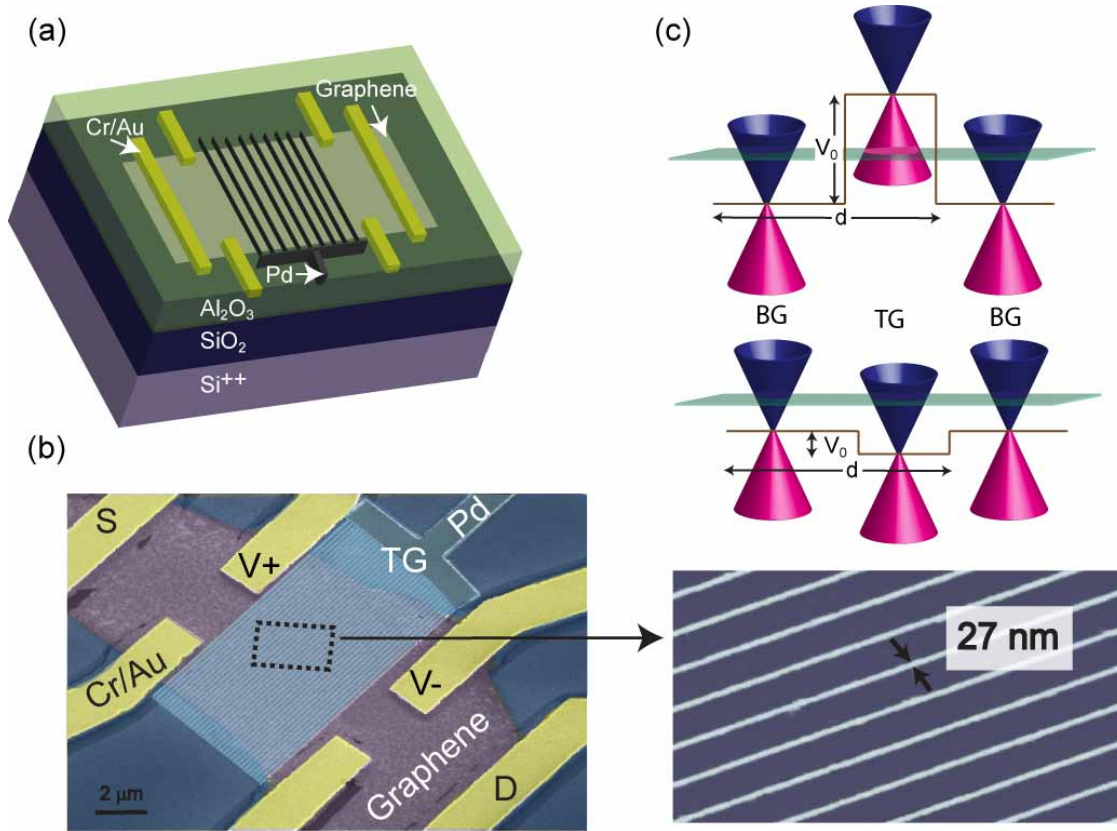


Figure 1: Device schematic to realize a lateral graphene SL. (a) Schematic of the device with a back-gate and a series of top-gates pinned to the same potential. This helps realize a regular periodic potential with ~ 40 periods. The substrate for the device is 300 nm thick silicon dioxide on degenerately doped silicon. The graphene flake is contacted by depositing 10 nm of Cr and 50 nm of Au. The top-gate dielectric is 23 nm of Al_2O_3 with 3 nm deposited by e-beam evaporation and 20 nm deposited using ALD. The top-gates are defined by electron beam lithography and by evaporating Pd. The width of top-gates is ~ 27 nm with a period of 150 nm. (b) False colored SEM image of a device in Hall bar geometry showing the device dimensions. The arrow points to a magnified view of the fingers of the top-gate structure. (c) Potential barriers created by alternate regions of local doping on a planar graphene device; this is realized using a back-gate and a series of top-gates pinned to the same potential. In the top figure, TG region is hole doped and BG region is electron doped and in the bottom figure both TG and BG region are electron doped with the green plane showing the Fermi energy.

can be divided into a series of alternating regions, one with only a back-gate (region denoted as BG) and the other that has both a top-gate (tg) and a back-gate (bg) (region denoted as TG) (see Figure 1c). The charge density in BG region is determined only by the applied back-gate voltage, while in the TG region, it is determined by both the back-gate voltage V_{bg} and the top-gate voltage V_{tg} , providing an independent control to set the charge carrier density and type in the two regions. The amplitude of the SL potential created is the difference in the charge neutral point between the BG and the TG region (illustrated in Figure 1c). The capacitive coupling of the top-gate (C_{tg}) is higher than that of the back-gate (C_{bg}) due to the geometrical proximity and higher dielectric constant of top-gate dielectric ($C_{tg}/C_{bg} = 18$) (see Section 4 of Supporting Information for details). Fringing fields from the top-gate electrodes lead to the smoothening of the SL potential and the effective width of the top-gate felt by the charge carriers in graphene is approximately 60-70 nm (details regarding the potential profile in Section 9 of the Supporting Information). Varying V_{tg} and V_{bg} , we probe the system having a series of p - n' - p (or n - p' - n) or p - p' - p (or n - n' - n) junctions depending on the combination of the two gate voltages, giving rise to a SL structure in graphene. The advantage of creating a SL structure using gate voltage is that the amplitude of the SL potential can be continuously varied, giving one control over the electronic properties, which is desirable for device applications. In addition, studies have suggested that around 10 periods of the SL are sufficient to see the effect of band formation;³⁸ in our experiments we have used ~ 40 periods of the SL.

The electrical properties of a monolayer graphene device (evidence for monolayer graphene provided in Section 2 of Supporting Information) are studied using a zero bias measurement. Figure 2a shows the colorscale plot of resistance measured at 300 mK as a function of V_{bg} and V_{tg} . The resistance of the device is low when charge carriers are of the same type in TG and BG region ($\text{sgn}(V_{bg}V_{tg})=1$) (top right and bottom left quadrant in Figure 2a). However, when the type of charge carriers in the two regions are different (this happens in part of the bottom right and top left quadrant of Figure 2a), we observe oscillations in resistance as a function of V_{tg} and V_{bg} . These oscillations fade in and out; their number increases with increasing gate voltage as seen in Fig-

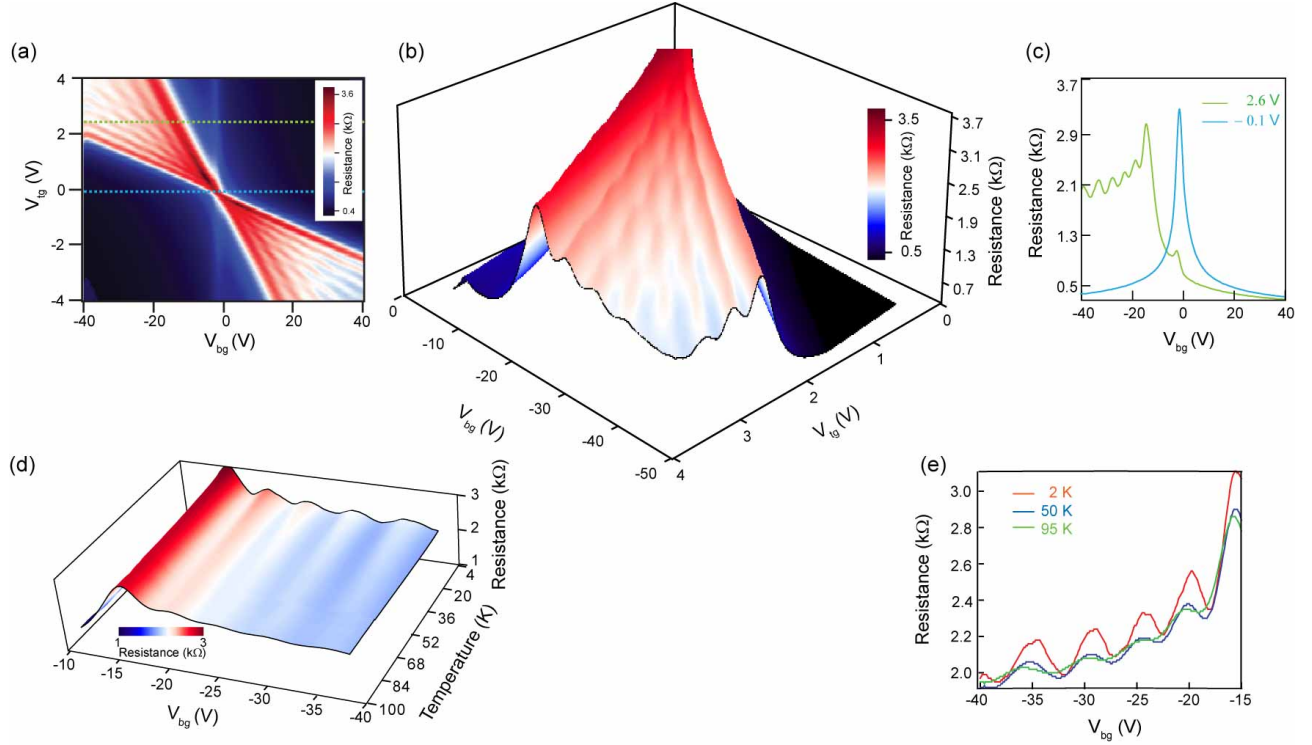


Figure 2: Electron transport measurements to probe the properties of the SL structure. (a) Resistance measured as a function of back-gate voltage V_{bg} and top-gate voltage V_{tg} at 300 mK. The oscillations in the resistance are seen when charge carriers in the TG and BG regions are of opposite sign. A positive (negative) sign of the gate voltage induces electrons (holes) in the system. The charge density in TG region is set by the algebraic sum of the effect of the voltages applied to the two gates. (b) A detailed measurement of the region of one of the quadrants shown in (a) where V_{bg} induces holes in the graphene sheet and V_{tg} induces electrons giving rise to a potential barrier of varying height at different points in the region. The splitting of resistance peaks as a function of the gate voltages is clearly observed. (c) Line plot of data shown in (a) at $V_{tg} = -0.1$ V (blue) and $V_{tg} = 2.6$ V (green). The line plot for $V_{tg} = 2.6$ V depicts oscillations. (d) Resistance as a function of V_{bg} and temperature with $V_{tg} = 2.6$ V showing that the oscillations persists even at around 70 K. (e) Line plot of resistance as a function of V_{bg} with $V_{tg} = 2.6$ V at three different temperatures.

ure 2b, which is a magnified and detailed measurement of one quadrant of Figure 2a. The number of resistance “ridges” increases by one as the magnitude of V_{tg} and V_{bg} is gradually increased. We note that increasing V_{bg} and V_{tg} in these quadrants amounts to increasing the superlattice barrier seen by the charge carrier and we discuss this aspect later in greater detail. Fixing V_{tg} at 2.6 V, resistance as a function of V_{bg} shows a distinct oscillatory pattern (as shown in green curve in Figure 2c). A slice of the data at the charge neutrality point shows a peak in the resistance at $V_{bg} = -2$ V as seen in the blue curve of Figure 2c. The field effect mobility of this device is $\sim 6000 \text{ cm}^2/(\text{Vs})$ at 300 mK and corresponds to a mean free path of ~ 70 nm (details regarding mobility calculation provided in Section 3 of Supporting Information). The presence of the array of top-gates does not significantly affect the mobility of the device (details in Section 3 of Supporting Information). Another aspect relevant for the transport properties of graphene devices is the depth of the charge puddles,^{39–42} U_{pud} , that result from the inhomogeneity of charge distribution. Here, $U_{pud} \sim 71$ meV (see Section 3 of Supporting Information) and is comparable with that seen by others in devices with similar mobility.

To further probe the energy and length scale related to the resistance oscillations, we study the transport as a function of temperature. Figure 2d shows the measurement of resistance with gate voltage and temperature (up to 100 K). The oscillations in resistance with gate voltage are robust against temperature and can be seen upto 100 K (8.3 meV), which provides an estimate of the relevant energy scale for the oscillations. The amplitude of the oscillations decrease with increasing temperature, as is clearly seen in the line plots taken at three different temperatures (Figure 2e). (Additional data on temperature variation of oscillations is shown in Section 6 of Supporting Information.)

We would like to note that the resistance oscillations are not as a result of coherent Fabry-Perot resonance of the SL, since the phase coherence $l_\phi \sim 0.6 \mu\text{m}$ at 300 mK (details provided in Section 5 of Supporting Information), whereas the SL periodicity is 150 nm. Therefore phase information is lost after 4 SL periods whereas in transport measurement we probe 40 SL periods. The fact that the oscillations persist upto 100 K, where l_ϕ is very small, indicates that the band

picture of SL rather than the coherent Fabry-Perot resonances is meaningful in understanding the oscillations in our experiment.

Having considered the experimental results, we now try to understand the potential profile created due to the combination of gates. To the first approximation, we assume that the potential created due to the top-gate is abrupt. The height of the potential created due to the top-gate and back-gate can be calculated from the doping in the two regions, with and without the top-gate; this amounts to measuring the shift in the charge neutrality point in the two regions.¹ The charge density induced by the back-gate is $C_{bg}V_{bg}$ and that by the top-gate is $C_{tg}V_{tg}$. The amplitude of the SL potential barrier V_0 is then given by (details in Section 8 of Supporting Information)

$$V_0 = \sqrt{\pi}\hbar v_F \left(\text{sgn}(C_{bg}V_{bg})\sqrt{\frac{|C_{bg}V_{bg}|}{e}} - \text{sgn}(C_{tg}V_{tg} + C_{bg}V_{bg})\sqrt{\frac{|C_{tg}V_{tg} + C_{bg}V_{bg}|}{e}} \right) \quad (1)$$

It is to be noted that for constant amplitude of the potential, in the bottom right quadrant of Figure 2a, we have electrons coming across barriers of constant height, and in the top left quadrant, holes face wells of constant depth. Since the measured data is symmetric, henceforth the magnitude of SL barrier (or well) is referred to as V_0 .

Introduction of the SL potential of period d introduces another energy scale $E_{SL} = (\hbar v_F/d)$ which controls the effect of the SL on the system and we examine the experimental results in units of E_{SL} . For our experiments, $d = 150$ nm and hence E_{SL} is ~ 4.4 meV. Following eq ??, Figure 3a shows a contour plot of V_0 as a function of V_{tg} and V_{bg} for the range of parameters used in our experiments with contours at $(V_0/E_{SL}) = 4\pi j$, where j is an integer. To understand the experimental results, we have taken slices of the experimental data along contours of constant V_0 . We take slices from the charge neutrality point and note that the charge neutrality point is influenced to some extent by both the gates due to fringing of fields resulting from the structure of the gates. Figure 3b shows the contours along which the slices are taken (dashed for holes corresponding to negative E_F) (additional slices are shown in Section 8 of Supporting Information).

Figure 3c,d shows slices of the data depicting longitudinal conductance (G_{xx}) for $(V_0/E_{SL}) =$

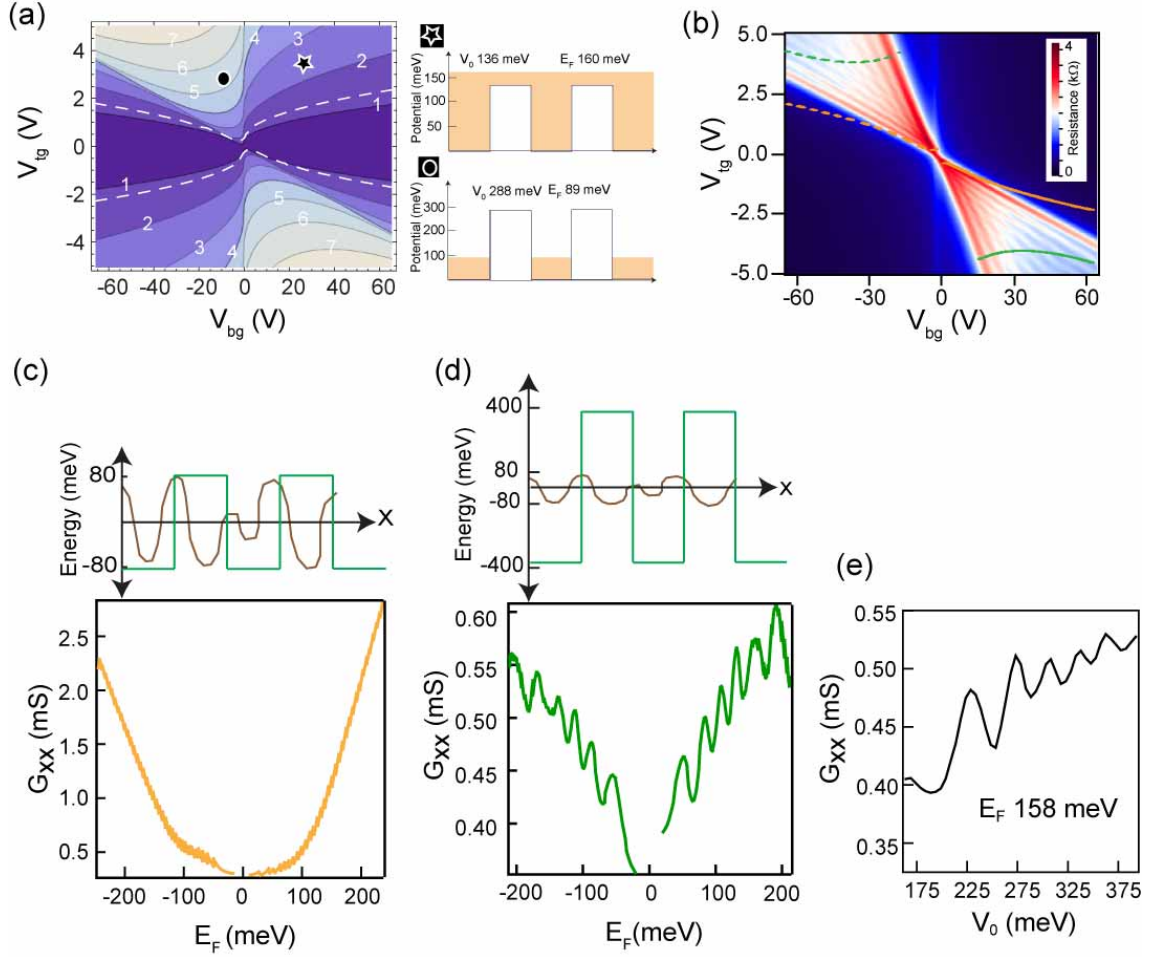


Figure 3: Effect of periodic potential on the transport. (a) Calculated height of potential barrier (V_0/E_{SL}) as a function of V_{tg} and V_{bg} where V_0 is given by eq ???. The plot shows contours of V_0/E_{SL} in units of 4π . The white dashed contour correspond to U_{pud} , and we observe effect of SL only when $V_0 \gg U_{pud}$. It is clear that the strength of the potential increases as the top-gate and back-gate strength increases to induce carriers of opposite sign (with $\text{sgn}(V_{tg}V_{bg})=-1$). Schematic on the side illustrates the height of the SL potential and the position of Fermi energy at two different regions denoted by star (region where oscillations are not observed) and circle (region where we see oscillations). (b) Experimentally measured resistance as a function of V_{tg} and V_{bg} with curves of constant V_0 . Contour of constant potential ($V_0/E_{SL} = 6\pi$ (in yellow) and ($V_0/E_{SL} = 26\pi$ (in green) overlaid on resistance as a function of V_{bg} and V_{tg} at 300 mK. This allows us to extract from experimentally measured data resistance variation at constant V_0 as a function of V_{bg} and consequently E_F . (c) Conductance as a function of E_F for ($V_0/E_{SL} = 6\pi$). (d) Conductance as a function of E_F for ($V_0/E_{SL} = 26\pi$). In this case, we see oscillations clearly as the potential created by the gate voltage is much greater than the typical potential variations due to electron hole puddles U_{pud} . (see Section 8 of Supporting Information for slices at various V_0 .) (e) Conductance as a function of V_0 at constant Fermi energy shows oscillatory behavior.

6π and 26π respectively. It can be seen from Figure 3c that for $(V_0/E_{SL}) = 6\pi$, we do not observe oscillations in G_{xx} as E_F is increased. However for higher V_0 , oscillations in G_{xx} become clearly visible as E_F is swept; an example of this is seen in Figure 3d for $(V_0/E_{SL}) = 26\pi$. The reason for this observation is the inhomogeneous charge distribution with $U_{pud} \sim 71$ meV (details regarding estimation about electron-hole puddles in graphene in Section 3 of Supporting Information). Because of the presence of puddles, the effects of the periodicity of the SL is not observed unless the depth of the potential modulation V_0 is much larger than U_{pud} ; this is illustrated by the cartoons in Figure 3c,d. Conductance as a function of V_0 at constant E_F also shows oscillatory behavior as seen in Figure 3e.

The relevance of E_{SL} is also observed in the temperature evolution of the resistance oscillations as seen in Figure 2d. For our experiment, $E_{SL} \sim 4.4$ meV, and we observe that the oscillations in resistance, both as a function of V_{tg} and V_{bg} , become indistinct around $100\text{ K} \approx 8.3$ meV. The observation that the resistance oscillations are suppressed when temperature exceeds E_{SL} and are seen only when $V_0 \gg U_{pud}$ shows that the resistance oscillations arise from the effect of SL potential and this serves as an internal consistency check.

We have already seen indirect experimental evidence (in the form of the energy scale set by the temperature dependence of the oscillations) that the presence of the SL is related to the resistance oscillations. We will now discuss how the SL modifies the graphene band structure, which leads to the experimentally observed resistance oscillations. Several approaches have been followed to study the effects of SL in monolayer and bilayer graphene.^{23–26,38} Here, we will follow the theoretical approach of Barbier *et al.*,²⁴ which obtains the band dispersion of Dirac particles in a square SL potential (with periodic variation along the length of the sample and a constant profile along the width) using a transfer matrix method. We would like to note that, although we use this specific method for ease of application, other approaches also provide very similar predictions.^{23–26,38} The band dispersion of the conduction band of the above mentioned Kronig Penny model for Dirac fermions is plotted as a function of the momentum in the y direction, k_y , for $k_x = 0$ in Figure 4a. From top to bottom, the three curves correspond to $V_0/E_{SL} = 18\pi, 22\pi$, and 26π , respectively. The

most dramatic modification of the graphene band structure brought about by the SL is the appearance of additional Dirac points (other than the one at $k_y = 0$), as seen in this figure. The number of additional Dirac points increase by 1 as V_0/E_{SL} is increased by 4π (e.g., from 18π which has four additional Dirac points to 22π , which has five additional Dirac points).

The relation between appearance of the Dirac points and the resistance oscillations can be understood by looking at the single particle density of states (DOS) calculated from the band dispersion, which is plotted in Figure 4b. The DOS oscillates with the energy (over and above a linearly increasing trend) with peaks corresponding to van Hove singularities occurring between the Dirac points. The number of these peaks follows the number of additional Dirac points in the spectrum and increase with increasing V_0 .

The DOS is related to the conductivity through the Einstein relation, $\sigma = e^2 v(E_F) D$, where D is the diffusion constant and $v(E_F)$ is the DOS at the Fermi level. In our samples, which have low mobility and hence are in the low diffusive limit where the localization length is much larger than the inter-carrier separation (see Section 10 of Supporting Information for details), the electrical conductivity is dominated by inelastic scattering processes, which allows hopping of the electrons from their localized (but overlapping) wavefunctions. In this case, on dimensional grounds, the diffusion constant $D \sim \alpha \xi_l^2 / \tau_{in}$, where α is a dimensionless constant, $\xi_l \gg k_F^{-1}$ is the localization length of the electrons and τ_{in} is the characteristic inelastic scattering time.⁴³ In this limit, the conductivity simply mimics the DOS at Fermi level. The resistance oscillations we observe are thus a reflection of the oscillation of the DOS with energy with the number of oscillations tracking the number of additional Dirac points produced in the spectrum by the SL.

In Figure 4c, we plot the experimentally measured conductance as a function of the Fermi energy of the charge carriers. We plot the theoretical data for DOS in Figure 4b and the experimental data for conductance in Figure 4c for the same values of V_0/E_{SL} (with the contours of constant V_0 shown in the V_{bg} - V_{tg} plane in Figure 4d) and see that they compare well with each other.

Qualitatively, both show a number of oscillations on top of a linearly increasing trend with the number increasing with increasing SL potential. We now proceed to a more quantitative com-

parison of the theoretical predictions and our experimental data, focusing chiefly on the period of oscillations observed in the two cases. The theoretical DOS oscillates with a period of ~ 21.1 meV, and the experimentally measured conductance oscillates with a period of ~ 27.9 meV. We would like to point out one major factor which can account for this difference, namely, the much smoother profile of the experimental superlattice potential compared to the abrupt square waveform of the Kronig Penny model used in the theory. Brey *et al.*³⁸ have studied the appearance of extra Dirac point with a smooth potential profile given by $V_0 \cos(2\pi x/d)$ and have found that the condition for appearance of new Dirac peaks is given by $J_0(V_0 d/2\pi\hbar v_F) = 0$. The successive Dirac peaks in this case appear when the SL potential is increased by $\sim 6.2\pi E_{SL} = 1.55(4\pi E_{SL})$. Thus the period can be significantly affected due to the smoothness of the potential profile. Because of finite thickness of the top gate dielectric, our device lies somewhere in between these two extreme limits. Thus the smoothness of the potential profile qualitatively explains the difference observed between the experimental observations and the theoretical predictions from the simple model. For a more accurate match of theory and experiment, one would have to solve for the dispersion using the actual potential profile of the device, but such calculation would not provide any new insight into the universal property of such devices.

Figure 4d summarizes the main experimental observation showing that as (V_0/E_{SL}) increases by $\sim 4\pi$, that is, as the number of extra Dirac points increases by one, the number of oscillations increases by one. Another remarkable feature in the data seen in the plot is that in the region of j extra Dirac points, the number of oscillations is j ; j being a positive integer.

In this work we have demonstrated a tunable SL resulting in controllable modification of the band structure. Besides electronic properties, such devices may be of interest for plasmonics and magnetic superlattices could be of interest for spintronic applications. SL structure modifying the band structure also opens ways to realize Weyl semimetal⁴⁴ predicted in topological insulators and for thermoelectric and spintronic applications.⁴⁵ Our work is a step towards exploring such devices.

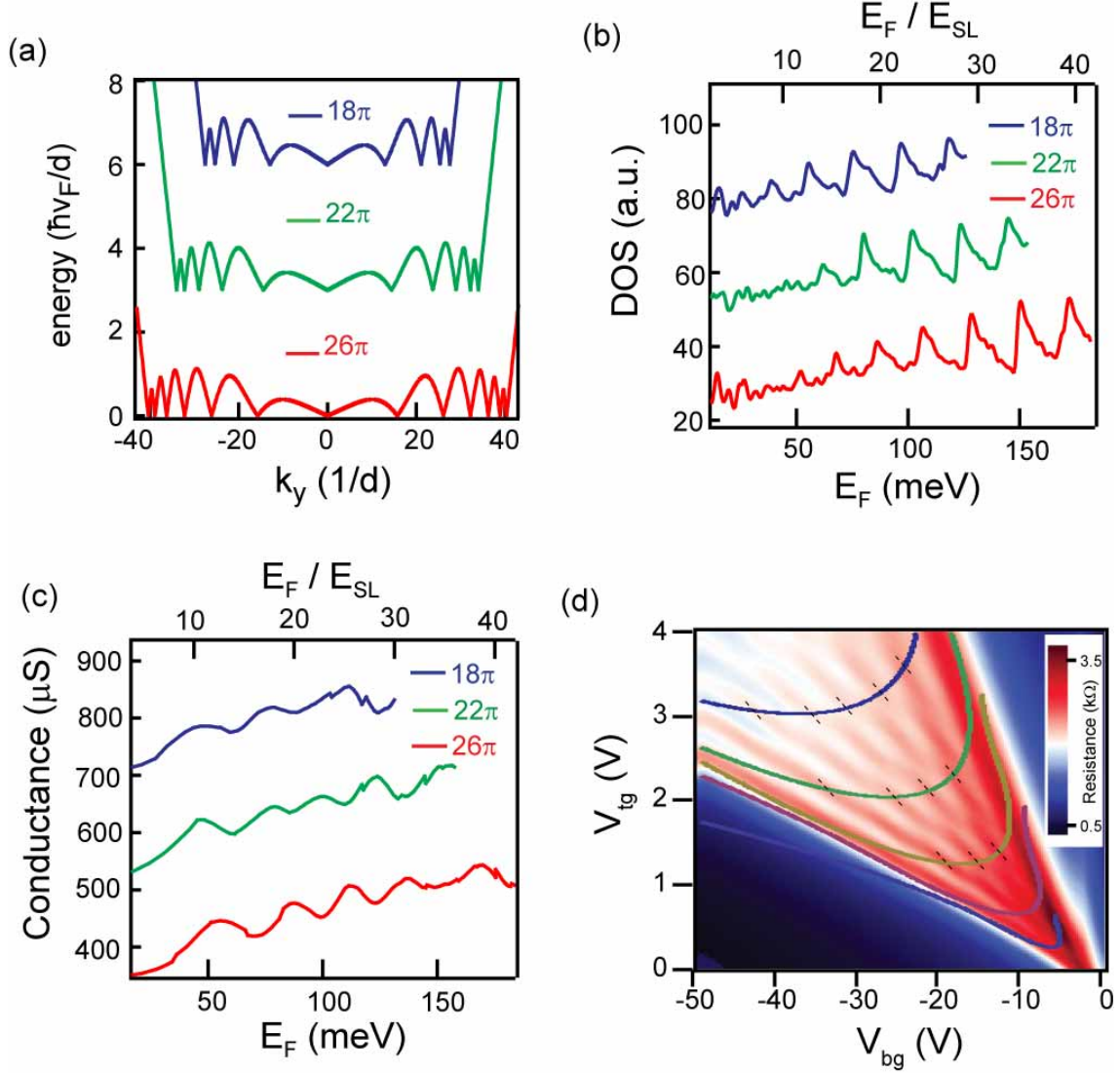


Figure 4: Modeling the transport through the SL and comparison with experimental results. (a) Calculated dispersion relation of the conduction band at $k_x = 0$ (x-direction is along the length of graphene and y-direction is along the width of graphene) for $V_0/E_{SL} = 18\pi$, 22π , and 26π . As SL potential increases the band bends increasing the number of Dirac points. The plots are offset by 3 units for clarity. (b) Calculated DOS as a function of E_F for the same strengths of potential (V_0/E_{SL}) as in (a). The plots are offset for clarity. DOS shows oscillations with an increasing trend with E_F and the number of oscillations increase with increasing SL potential. (c) Plot of measured conductance as a function of Fermi energy for same value of (V_0/E_{SL}) as in (a,b). The plot for (V_0/E_{SL}) at 22π and 18π is shifted by $200 \mu S$ and $400 \mu S$, respectively, for clarity. Similar to the oscillations observed in (a), we see an increasing trend in oscillations with E_F and that their number increases with increasing SL potential. (d) Contours of constant V_0 separated by $4\pi E_{SL}$ overlaid on measured resistance as a function of V_{bg} and V_{tg} . Contours are calculated using the model of square SL. These contours pass approximately through the local peaks (shown by the black dotted line) showing that the number of oscillations increases by one as we cross the region of V_0 where one more extra Dirac point is created. We also observe that in the region of j extra Dirac points, the number of oscillations is j , j being a positive integer.

Acknowledgement

We thank Professor Jim Eisenstein for helpful discussions, Dr. Abhilash T.S. for help with the measurement setup and Tanuj Prakash for help with fabrication. We thank Dr. Michael Barbier for sharing the scheme of their calculation. We acknowledge Swarnajayanthi Fellowship of Department of Science and Technology and Department of Atomic Energy of Government of India for support.

References

- (1) Katsnelson, M. I.; Novoselov, K. S.; Geim, A. K. *Nat. Phys.* **2006**, 2, 620–625.
- (2) Shytov, A. V.; Rudner, M. S.; Levitov, L. S. *Phys. Rev. Lett.* **2008**, 101, 156804.
- (3) Klein, O. Z. *Phys.* **1929**, 53, 157–165.
- (4) Novoselov, K. S.; Geim, A. K.; Morozov, S. V.; Jiang, D.; Katsnelson, M. I.; Grigorieva, I. V.; Dubonos, S. V.; Firsov, A. A. *Nature* **2005**, 438, 197–200.
- (5) Zhang, Y.; Tan, Y.; Stormer, H. L.; Kim, P. *Nature* **2005**, 438, 201–204.
- (6) Bolotin, K. I.; Ghahari, F.; Shulman, M. D.; Stormer, H. L.; Kim, P. *Nature* **2009**, 462, 196–199.
- (7) Du, X.; Skachko, I.; Duerr, F.; Luican, A.; Andrei, E. Y. *Nature* **2009**, 462, 192–195.
- (8) Chen, J.; Badioli, M.; Alonso-González, P.; Thongrattanasiri, S.; Huth, F.; Osmond, J.; Spasenović, M.; Centeno, A.; Pesquera, A.; Godignon, P.; Elorza, A. Z.; Camara, N.; Abajo, F. J. G. d.; Hillenbrand, R.; Koppens, F. H. L. *Nature* **2012**, 487, 77–81.
- (9) Fei, Z.; Rodin, A. S.; Andreev, G. O.; Bao, W.; McLeod, A. S.; Wagner, M.; Zhang, L. M.; Zhao, Z.; Thiemens, M.; Dominguez, G.; Fogler, M. M.; Neto, A. H. C.; Lau, C. N.; Keilmann, F.; Basov, D. N. *Nature* **2012**, 487, 82–85.

- (10) Yan, H.; Li, X.; Chandra, B.; Tulevski, G.; Wu, Y.; Freitag, M.; Zhu, W.; Avouris, P.; Xia, F. *Nat. Nanotechnol.* **2012**, *7*, 330–334.
- (11) Koppens, F. H. L.; Chang, D. E.; García de Abajo, F. J. *Nano Lett.* **2011**, *11*, 3370–3377.
- (12) Lee, J. M.; Choung, J. W.; Yi, J.; Lee, D. H.; Samal, M.; Yi, D. K.; Lee, C.-H.; Yi, G.-C.; Paik, U.; Rogers, J. A.; Park, W. I. *Nano Lett.* **2010**, *10*, 2783–2788.
- (13) Gorbachev, R. V.; Geim, A. K.; Katsnelson, M. I.; Novoselov, K. S.; Tudorovskiy, T.; Grigorieva, I. V.; MacDonald, A. H.; Morozov, S. V.; Watanabe, K.; Taniguchi, T.; Ponomarenko, L. A. *Nat. Phys.* **2012**, *8*, 896–901.
- (14) Novoselov, K. S.; Fal’ko, V. I.; Colombo, L.; Gellert, P. R.; Schwab, M. G.; Kim, K. *Nature* **2012**, *490*, 192–200.
- (15) Liu, M.; Yin, X.; Ulin-Avila, E.; Geng, B.; Zentgraf, T.; Ju, L.; Wang, F.; Zhang, X. *Nature* **2011**, *474*, 64–67.
- (16) Wu, Y.; Lin, Y.-m.; Bol, A. A.; Jenkins, K. A.; Xia, F.; Farmer, D. B.; Zhu, Y.; Avouris, P. *Nature* **2011**, *472*, 74–78.
- (17) Xia, F.; Mueller, T.; Lin, Y.-m.; Valdes-Garcia, A.; Avouris, P. *Nat. Nanotechnol.* **2009**, *4*, 839–843.
- (18) Konstantatos, G.; Badioli, M.; Gaudreau, L.; Osmond, J.; Bernechea, M.; Arquer, F. P. G. d.; Gatti, F.; Koppens, F. H. L. *Nat. Nanotechnol.* **2012**, *7*, 363–368.
- (19) Elias, D. C.; Nair, R. R.; Mohiuddin, T. M. G.; Morozov, S. V.; Blake, P.; Halsall, M. P.; Ferrari, A. C.; Boukhvalov, D. W.; Katsnelson, M. I.; Geim, A. K.; Novoselov, K. S. *Science* **2009**, *323*, 610–613.
- (20) Li, X.; Wang, X.; Zhang, L.; Lee, S.; Dai, H. *Science* **2008**, *319*, 1229–1232.
- (21) Pereira, V. M.; Castro Neto, A. H.; Peres, N. M. R. *Phys. Rev. B* **2009**, *80*, 045401.

- (22) Tsu, R.; Esaki, L. *Appl. Phys. Lett.* **1973**, *22*, 562–564.
- (23) Park, C.-H.; Yang, L.; Son, Y.-W.; Cohen, M. L.; Louie, S. G. *Nat. Phys.* **2008**, *4*, 213–217.
- (24) Barbier, M.; Vasilopoulos, P.; Peeters, F. M. *Phys. Rev. B* **2010**, *81*, 075438.
- (25) Killi, M.; Wu, S.; Paramakanti, A. *Phys. Rev. Lett.* **2011**, *107*, 086801.
- (26) Burset, P.; Yeyati, A. L.; Brey, L.; Fertig, H. A. *Phys. Rev. B* **2011**, *83*, 195434.
- (27) Killi, M.; Wu, S.; Paramakanti, A. *Int. J. Mod. Phys. B* **2012**, *26*, 1242007.
- (28) Young, A. F.; Kim, P. *Ann. Rev. Condens. Matter Phys.* **2011**, *2*, 101–120.
- (29) Tan, L. Z.; Park, C.-H.; Louie, S. G. *Nano Lett.* **2011**, *11*, 2596–2600.
- (30) Park, C.-H.; Yang, L.; Son, Y.-W.; Cohen, M. L.; Louie, S. G. *Phys. Rev. Lett.* **2008**, *101*, 126804.
- (31) Park, C.-H.; Son, Y.-W.; Yang, L.; Cohen, M. L.; Louie, S. G. *Nano Lett.* **2008**, *8*, 2920–2924.
- (32) Ho, J. H.; Chiu, Y. H.; Tsai, S. J.; Lin, M. F. *Phys. Rev. B* **2009**, *79*, 115427.
- (33) Yankowitz, M.; Xue, J.; Cormode, D.; Sanchez-Yamagishi, J. D.; Watanabe, K.; Taniguchi, T.; Jarillo-Herrero, P.; Jacquod, P.; LeRoy, B. J. *Nat. Phys.* **2012**, *8*, 382–386.
- (34) Ponomarenko, L. A.; Gorbachev, R. V.; Yu, G. L.; Elias, D. C.; Jalil, R.; Patel, A.; Mishchenko, A.; Mayorov, A. S.; Woods, C. R.; Wallbank, J.; Mucha-Kruczynski, M.; Piot, B. A.; Potemski, M.; Grigorieva, I. V.; Novoselov, K. S.; Guinea, F.; Fal'ko, V. I.; Geim, A. K. *Nature* **2013**, *497*, 594–597
- (35) Dean, C. R.; Wang, L.; Maher, P.; Forsythe, C.; Ghahari, F.; Gao, Y.; Katoch, J.; Ishigami, M.; Moon, P.; Koshino, M.; Taniguchi, T.; Watanabe, K.; Shepard, K. L.; Hone, J.; Kim, P. *Nature* **2013**, *497*, 598–602

- (36) Pletikosić, I.; Kralj, M.; Pervan, P.; Brako, R.; Coraux, J.; N'Diaye, A. T.; Busse, C.; Michely, T. *Phys. Rev. Lett.* **2009**, *102*, 056808.
- (37) Carozo, V.; Almeida, C. M.; Ferreira, E. H. M.; Cançado, L. G.; Achete, C. A.; Jorio, A. *Nano Lett.* **2011**, *11*, 4527–4534.
- (38) Brey, L.; Fertig, H. A. *Phys. Rev. Lett.* **2009**, *103*, 046809.
- (39) Martin, J.; Akerman, N.; Ulbricht, G.; Lohmann, T.; Smet, J. H.; Klitzing, K. v.; Yacoby, A. *Nat. Phys.* **2008**, *4*, 144–148.
- (40) Deshpande, A.; Bao, W.; Miao, F.; Lau, C. N.; LeRoy, B. J. *Phys. Rev. B* **2009**, *79*, 205411.
- (41) Rossi, E.; Das Sarma, S. *Phys. Rev. Lett.* **2008**, *101*, 166803.
- (42) Dean, C. R.; Young, A. F.; Meric, I.; Lee, C.; Wang, L.; Sorgenfrei, S.; Watanabe, K.; Taniguchi, T.; Kim, P.; Shepard, K. L.; Hone, J. *Nat. Nanotechnol.* **2010**, *5*, 722–726.
- (43) Thouless, D. *Solid State Commun.* **1980**, *34*, 683–685.
- (44) Burkov, A. A.; Balents, L. *Phys. Rev. Lett.* **2011**, *107*, 127205.
- (45) Song, J.-H.; Jin, H.; Freeman, A. J. *Phys. Rev. Lett.* **2010**, *105*, 096403.